Galvanic Restructuring of Exsolved Nanoparticles for Plasmonic and Electrocatalytic Energy Conversion

Xiaolan Kang, Vilde Mari Reinertsen, Kevin Gregor Both, Augustinas Galeckas, Thomas Aarholt, Øystein Prytz, Truls Norby, Dragos Neagu, and Athanasios Chatzitakis*

There is a growing need to control and tune nanoparticles (NPs) to increase their stability and effectiveness, especially for photo- and electrochemical energy conversion applications. Exsolved particles are well anchored and can be re-shaped without changing their initial location and structural arrangement. However, this usually involves lengthy treatments and use of toxic gases. Here, the galvanic replacement/deposition method is used, which is simpler, safer, and leads to a wealth of new hybrid nanostructures with a higher degree of tailorability. The produced NiAu bimetallic nanostructures supported on $SrTiO_3$ display exceptional activity in plasmon-assisted photoelectrochemical (PEC) water oxidation reactions. In situ scanning transmission electron microscopy is used to visualize the structural evolution of the plasmonic bimetallic structures, while theoretical simulations provide mechanistic insight and correlate the surface plasmon resonance effects with structural features and enhanced PEC performance. The versatility of this concept in shifting catalytic modes to the hydrogen evolution reaction is demonstrated by preparing hybrid NiPt bimetallic NPs of low Pt loadings on highly reduced $SrTiO_3$ supports. This powerful methodology enables the design of supported bimetallic nanomaterials with tunable morphology and catalytic functionalities through minimal engineering.

X. Kang, K. G. Both, T. Norby, A. Chatzitakis
Centre for Materials Science and Nanotechnology
Department of Chemistry
University of Oslo
Gaustadalléen 21, Oslo NO-0349, Norway
E-mail: athanasios.chatzitakis@smn.uio.no
V. M. Reinertsen, A. Galeckas, T. Aarholt, Ø. Prytz
Centre for Materials Science and Nanotechnology
Department of Physics
University of Oslo
P. O. Box 1048 Blindern, Oslo NO-0316, Norway
D. Neagu
Department of Chemical and Process Engineering
University of Strathclyde
75 Montrose St, Glasgow G1 1XJ, UK

The ORCID identification number(s) for the author(s) of this article can be found under https://doi.org/10.1002/smll.202201106.

1. Introduction

Metallic nanoparticles (NPs) are crucial in a broad range of applications, such as catalysis, photo-catalysis, plasmonics, electronics, sensors, and photovoltaics.[1] Generally, their properties and targeted functionalities can be tuned by adjusting parameters such as structure, morphology, and composition.[2] More specifically, bimetallic NPs exhibit unique properties outperforming their monometallic counterparts, as is the case for Ir–Ru bimetallic composites, which are efficient and stable electrocatalysts for the oxygen evolution reaction (OER) in acidic solutions.[1b] Another example is Pd–Ag bimetallic structures, which can increase the selectivity in the hydrogenation of ethylene compared to the widely used Pd or Ag monomers, a fact attributed to modulation of hydrogen adsorption on Pd in the composites.[3] Bimetallic composites involving plasmonic metals, like Au, Ag, Cu, and Al are of particular interest because of the localized surface plasmon resonance (LSPR) effect,[4] which renders them important photosensitizers in semiconductor-supported systems for photocatalytic and photoelectrochemical (PEC) applications.[5] Recently, the antenna–reactor effect has been demonstrated, in which plasmonic NPs (antenna) induce a localized field that can significantly enhance the catalytic reaction rates on adjacent NPs (reactor).[6] This system has the advantage of combining the optical response of plasmonically active metals and the catalytic abilities of catalytically active metals.

The synthesis of such supported multi-metallic NPs with targeted structural features is hence of great importance, but very challenging. Most of the approaches developed so far involve co-reduction or co-precipitation, in situ exsolution, galvanic replacement reaction (GRR), Ostwald ripening and Kirkendall effects.[2d,7] Among them, GRR stands out due to its simplicity and versatility in engineering the metallic nanostructures in terms of composition, morphology, structure, etc.[8] GRR is a chemical process in which one metal often referred to as the sacrificial template is oxidized by the ions of another metal. The standard reduction potential difference between the sacrificial and depositing metals provides the driving force for the galvanic deposition of the desired metallic element.[9]

**ADVANCED
SCIENCE NEWS**

www.advancedsciencenews.com

NANO · MICRO

small

www.small-journal.com

In situ exsolution is a facile process to prepare well-defined and anchored supported NPs. In this process, the catalytically active metal elements are initially dissolved into the host oxide lattice during the crystallization process, and then partly exsolved from the support upon subsequent reductive conditions.[10] Exsolved metallic NPs with lower reduction potentials are excellent templates for subsequent GRR reactions and the formation of new structures and enhanced functionalities.

Here we show how the combination of two powerful methods as in situ exsolution and galvanic replacement forms a new method of chemical (solid-ion reaction) restructuring and hybridization of supported bimetallic NPs. These new and otherwise impossible to form exotic nanostructures supported on perovskite oxides ($SrTiO_3$) have tunable catalytic functionalities and are prepared with minimal engineering requirements.[8b,11] Specifically, we deposit through the galvanic replacement reaction plasmonic Au nano-islands on exsolved Ni NPs and both experimental evidence and modeling data correlate the improved PEC water splitting performance to the localized surface plasmon resonance of Au, as well as to the synergetic effect between Ni and Au in the form of antenna–reactor. We shift the catalytic activity of the parent compound by galvanically depositing Pt that forms Pt nano-needles with superior hydrogen evolution rate (HER) activity, approaching that of commercial Pt/C in alkaline media, with considerably lower Pt loadings.

2. Results

2.1. Crystal Structures and the Evolution of As-Prepared Samples

An overview of the different synthesis conditions and the corresponding obtained structures is schematically presented in **Figure 1**. La- and Ni- co-doped, A-site deficient $SrTiO_3$ ($La_{0.6}Sr_{0.2}Ti_{0.9}Ni_{0.1}O_{3-x}$ – LSTN, refer also to Note S1, Supporting Information) was first reduced in H_2 atmosphere (rLSTN) or in the presence of CaH_2 (rLSTN-CaH_2) to get Ni exsolution. We have previously studied the reduction of TiO_2 in the presence of CaH_2 and we showed that heavily reduced TiO_2 nanotube films with metallic conductivity could be obtained.[12] Motivated by this, we successfully exsolved Ni NPs in the presence of CaH_2 at as low temperatures as 600 °C. Then, the galvanic replacements were done by exposing rLSTN to a Au (III) complex solution (rLSTNAu) and the rLSTN-CaH_2 to a Pt (IV) solution to form, respectively, ladybug-like NiAu bimetallic and hedgehog-like NiPt supported, hybrid nanostructures. In this way, we can tune the electrocatalytic activity of the parent compound from plasmon-assisted photoelectrocatalytic water splitting to electrocatalysis for the HER. Details of the synthesis steps are given in the supporting information (SI), but the main structures are discussed below.

We examined the crystal structures of the as-synthesized LSTN, rLSTN, and rLSTNAu samples by X-ray diffraction (XRD). As displayed in **Figure 2**a, the XRD patterns of these three samples are almost identical (single phase cubic structure, $Pm\overline{3}m$) showing a high degree of crystallinity, that indicates the stability of LSTN upon high temperature chemical reduction and galvanic replacement reactions. The

characteristic peak of metallic Ni at ≈44.5º (inset II) is detectable in the XRD patterns of rLSTN and rLSTNAu but not in the LSTN, as expected. After the galvanic replacement reaction with the Au (III) complex solution, a new peak is detected at ≈38.3º (inset I) of the rLSTNAu sample, which is indexed to cubic metallic Au.[13]

Dopants (Ni and La) and deficiencies (A-site deficiency and oxygen non-stoichiometry) deliberately introduced in these compositions to promote exsolution, led to a slight distortion to the perovskite structure. A close examination of the (222) reflection (≈86.4º, inset IV, cubic primitive cell) shows a small shoulder peak at higher angle, indicating the increased pseudocubic unit cell parameter (a_p) and lattice distortion after Ni doping. Such a shoulder peak becomes invisible after reduction, but a peak-shifting of both the (202) (≈67.9º, inset III) and (222) reflections toward lower angles is observed for the rLSTN and rLSTNAu samples. The lattice parameters were estimated by Rietveld refinement ($Pm\overline{3}m$, a_p (LSNT): 3.8969 Å, a_p (rLSNT): 3.8978 Å, refer to Figure S1, Supporting Information for fitted data), where the slight lattice expansion after reduction can be attributed to the egress of Ni dopants from the parent lattice accompanied by the formation of oxygen vacancies. Besides, the Ti^{4+} radius in the oxidized LSTN is generally 0.605 Å, while the reduced rLSTN contains traces of Ti^{3+} with an ionic radius of 0.670 Å, further expanding of the cell parameters.[14]

Figure 2b–f displays the microstructures of the as-prepared samples. LSTN shows a relatively smooth surface, as seen in Figure 2b, but after reduction, nano-sized particles are exsolved, resulting in a rough surface of rLSTN (Figure 2c). The scanning transmission electron microscopy (STEM) image and the corresponding energy dispersive spectroscopy (EDS) mapping of rLSTN (Figure 1g and inset) further confirm the homogeneous dispersion of Ni NPs on the perovskite surface. The exsolution on both surface and grain boundaries are observed in the rLSTN sample, which exhibits major differences in terms of NPs size and population: the exsolved NPs inside the grain are much smaller and more numerous compared to the ones on the surface, which reflects different nucleation and growth rates, maybe related to strain associated with the NPs growing within the bulk. More scanning electron microscope (SEM) images corresponding to additional investigations showing exsolved particles of different sizes and surface population relative to changes in reduction temperature and duration are presented in Figure S2 (Supporting Information), while bulk exsolution SEM images are shown in Figure S3 (Supporting Information). Previous studies have already shown this phenomenon and suggested that embedding metal NPs within non-metallic crystal lattices improves the electronic transport in a manner analogous to substitutional aliovalent doping.[15]

Figure 2d–f give an overview of the obtained NiAu bimetallic NPs anchored on the surface of the perovskite hosts after the galvanic replacement reaction. We emphasize that the freshly-made sample shows a ladybug-like morphology, where many small Au NPs (≈2 nm) decorate one Ni particle (Figure 2d), as well as an antenna–reactor-like structure (Figure 2e). The ladybug structure is of high surface energy and a coalescence of the Au NPs takes place, evolving to a nanoflower structure (Figure 2f; Figure S4, Supporting Information) under ambient conditions, typically in the range of several hours to a few days
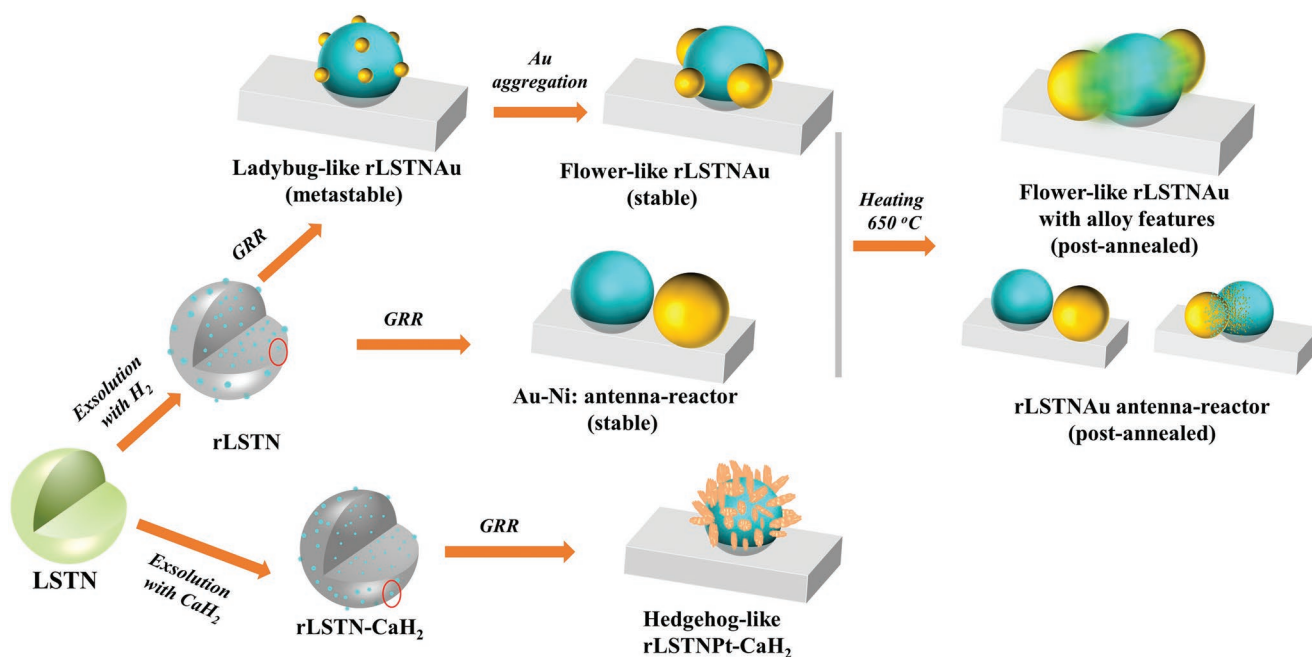
Figure 1. Schematic representation of the observed evolution of NiAu and NiPt bimetallic NPs. Ni exsolution was achieved in H_2 atmosphere (rLSTN) or by CaH_2 (rLSTN-CaH_2). The exsolved Ni NPs were partly replaced by Au or Pt to obtain a mixture of ladybug-like and antenna–reactor rLSTNAu and hedgehog-like rLSTNPt-CaH_2 structures, respectively. The ladybug-like rLSTNAu evolved into the flower-like structure. A subsequent short-time thermal treatment further evolved the different structures, inducing slight alloy features.

after the material is exposed to air. A characteristic STEM image and accompanying energy dispersive spectroscopy (EDS) analysis of a NiAu nanoflower structure can be seen in Figure 2h,i. Additional SEM images of all the structures are shown categorized in Figure S5 (Supporting Information), also being transformed into the corresponding color plots of Figure S6 (Supporting Information). From the color plots we were able to extract the Au and Ni NPs sizes distribution, which are summarized by category in Figure S7 (Supporting Information). In general, we see that the diameter of the Au NPs increases from the ladybug to the flower-like and to the post-annealed structures. The antenna–reactor structures contain the largest in diameter Au NPs and our analysis indicates that the ratio between flower-like:antenna–reactor in both the pre and post annealed rLSTNAu is ≈5:1. Finally, the Au NPs appear overall larger than the Ni NPs, which is expected as they are partially covered by Au NPs.

2.2. Structural Evolution of the rLSTNAu and In Situ Scanning Transmission Electron Microscopy Studies

Structures in the forms of hollow structures, core–shell, yolk–shell, and alloys are the general products of GRR,[8b] but the unique metastable ladybug and flower-like shapes in this study are new. Controlling the selective formation of these structures is challenging, but this creates a new landscape in the synthesis of supported multi-metallic NPs. Currently, they might have derived from i) the high degree of bulk immiscibility between Ni and Au caused by the large lattice mismatch (≈15.7%) and the weak adhesive interaction,[16] and/or ii) corrosion pits on

the native and naturally occurring surface oxides/hydroxide on the Ni NPs,[17] as it can also be seen in Figure S8 (Supporting Information), which shows the presence of oxygen on the Ni NP. In spite of the large difference in the reduction potential between metallic Ni and $AuCl_4^-$, Ni atoms first have to migrate through the self-passivating oxide shell, reach the surface and then participate in GRR, which significantly increases the energy barrier. Therefore, the growth of the Au nucleus into a nanoparticle becomes more favorable than forming core-shell or alloy structures on the amorphous surface of Ni oxide. Alternatively, the acidity of the GRR solution may etch away the native oxide/hydroxide layer and form corrosion pits that cause the galvanic Au deposition in the ladybug-like form.

Furthermore, the antenna–reactor-like structure might originate from the coalescence of smaller Au NPs as for the flower-like ones, but only resulting in one Au NP next to the Ni NP. Another possible explanation could be that rLSTN is also participating in the GRR. We have recently shown that when heavily reduced TiO_2 (black TiO_2) was immersed in a solution of Pt (IV) ions, then a spontaneous deposition of well-formed Pt NPs occurred.[18] Our experimental evidence as well as density functional theory (DFT) studies suggest that neutral oxygen vacancies donate electrons to Pt (IV) that consequently grows to Pt NPs of an average diameter of 2 nm. Similarly, this may be the case with the rLSTN sample and nucleation site adjacent to the Ni NPs. Extracting the mechanism behind these transformations, as well as the stabilization of the high energy ladybug-like structures requires further studies.

To gain a better insight into the structural evolution of the rLSTNAu sample (Figure 2), we subjected it to thermal annealing under high vacuum using an in situ sample holder
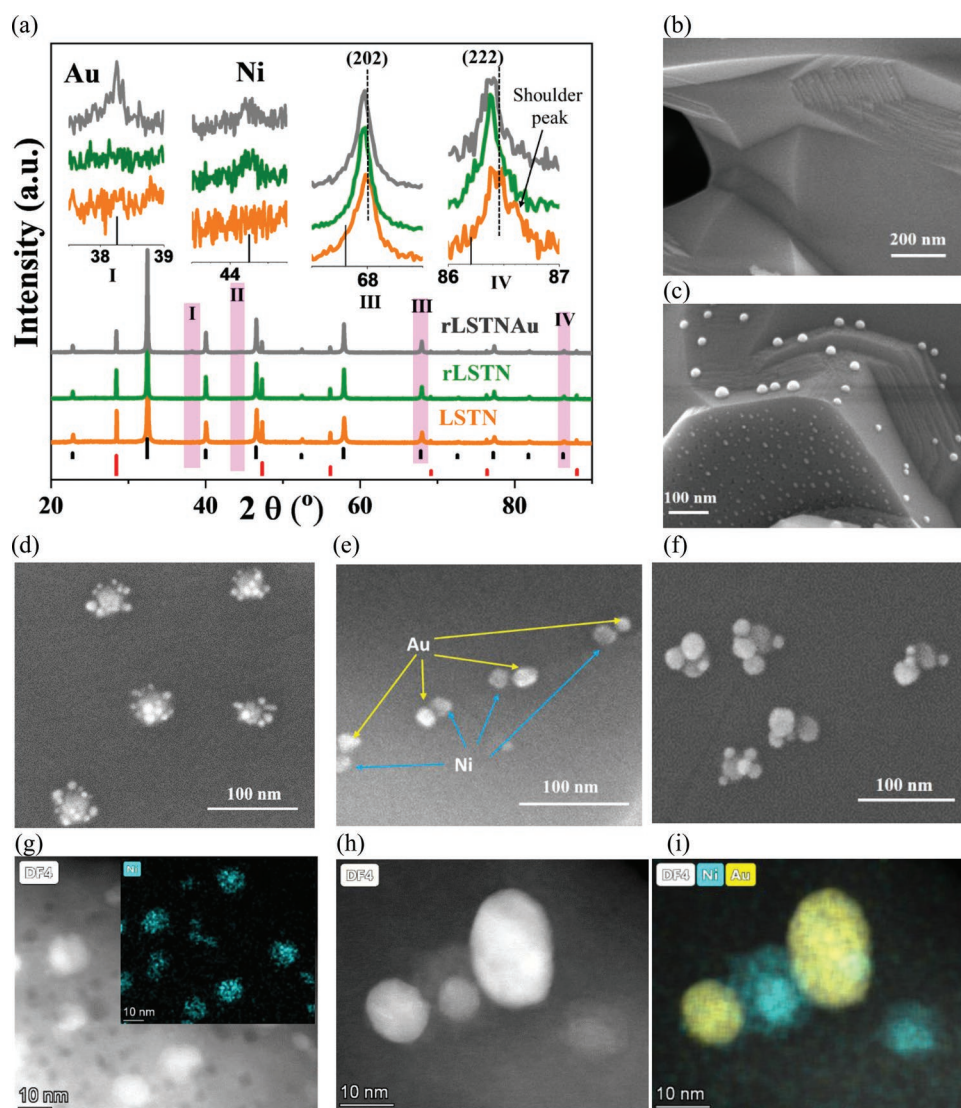
Figure 2. Structural characterization of the nano-engineered LSTN precursor material. a) XRD patterns of LSTN, rLSTN, and rLSTNAu. All the diffractograms are normalized on a scale from 0 to 1. Insets are the enlarged peaks in the specified 2θ angles. The lines underneath the XRD patterns denote the expected peak positions of $SrTiO_3$ (cubic, ICSD 65088, in black) and Si (cubic, ICSD 257794, in red), b) SEM images of LSTN before and c) after exsolution (rLSTN) at 900 °C. d) rLSTNAu after GRR in the metastable ladybug structure. e) rLSTNAu antenna–reactor structure. f) rLSTNAu flower-like structure. g) DF-STEM image of rLSTN and the corresponding EDS mapping of Ni (inset). h) STEM-DF4 pattern of NiAu nanocomposite embedded on perovskite surface, i) the corresponding EDS mapping of the flower-like NiAu structure.

for STEM. It is well-known that binary nanocrystals with various structures (e.g., alloy, core-shell and heterostructure) generally display distinct physical and chemical properties, which further give rise to different performance during reactions.[19] In our case and as displayed in **Figure 3** and Figure S4 (Supporting Information), the flower-like shape gradually developed also a NiAu alloy-containing structure in the post annealed rLSTNAu sample.[20]

The magnified STEM-DF images and the EDS mapping displayed in Figure 3 reveal that Ni and Au NPs stand side by side before heat treatment. It is noted that the snapshots were taken during this dynamic process, reflecting more accurately the structural changes occurring. As the temperature increases to 200 °C, the structural change of Ni and Au NPs is insignificant.

A coalescence between particles occurred at 300 °C, where Au appears to diffuse on the surface of rLSTN and wrap around the Ni NPs. A more significant reconstruction begins at 400 °C with an Au layer partially covering the Ni surface. This wrapping might be attributed to the removal of oxygen atoms from the thin NiO layer, leading to the amorphous reconstruction of Ni and Au atoms with partial interdiffusion between Au and Ni atoms.

The above observations demonstrate the outstanding anchorage of exsolved Ni at the perovskite surface, as well as the simple yet intriguing reconstruction of Au around Ni particles. Finally, and already at 600 °C, a partial diffusion of Au atoms into the Ni NPs is seen, accompanied by a slight alloying morphology at higher temperatures (650 °C).[19,20]
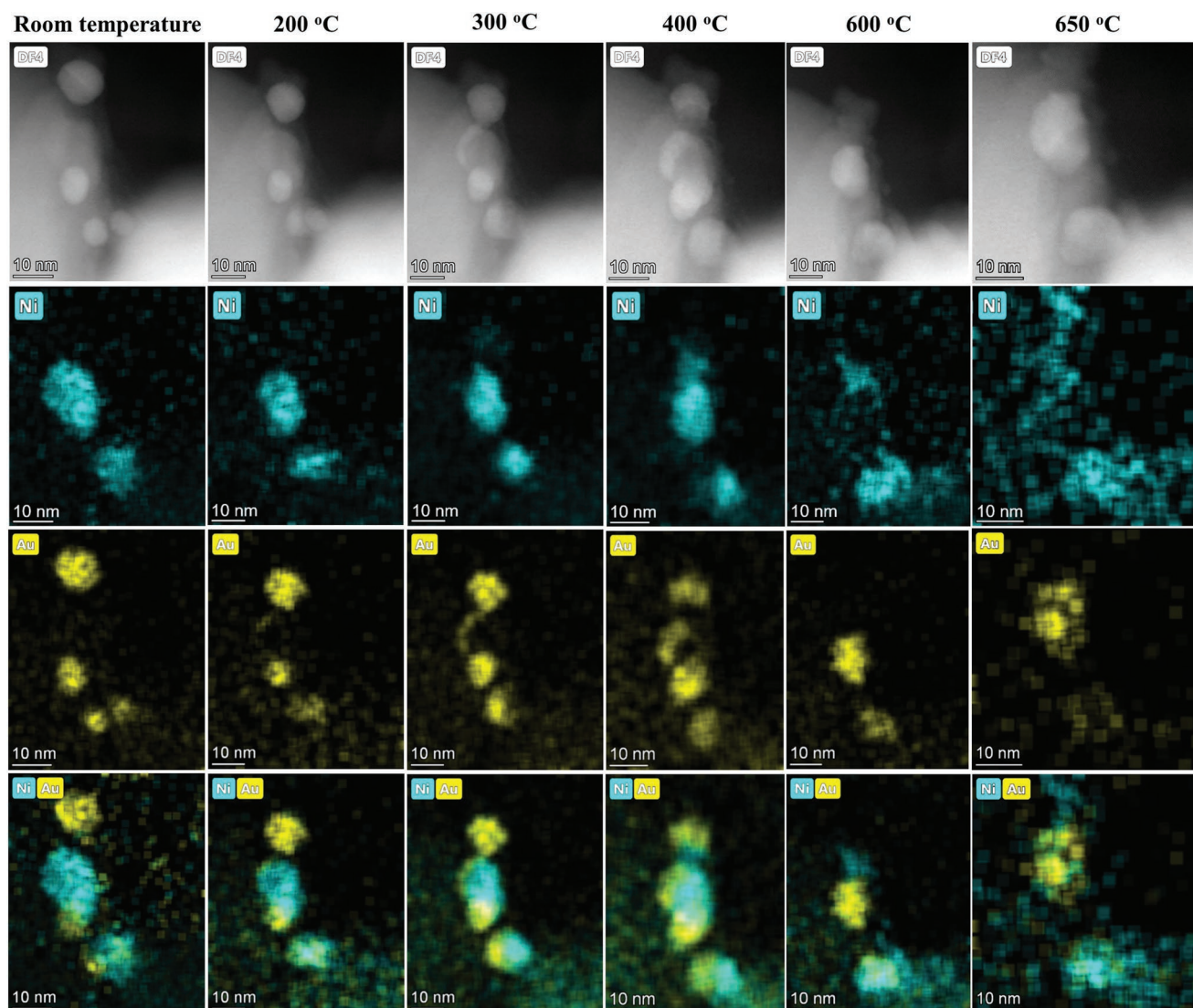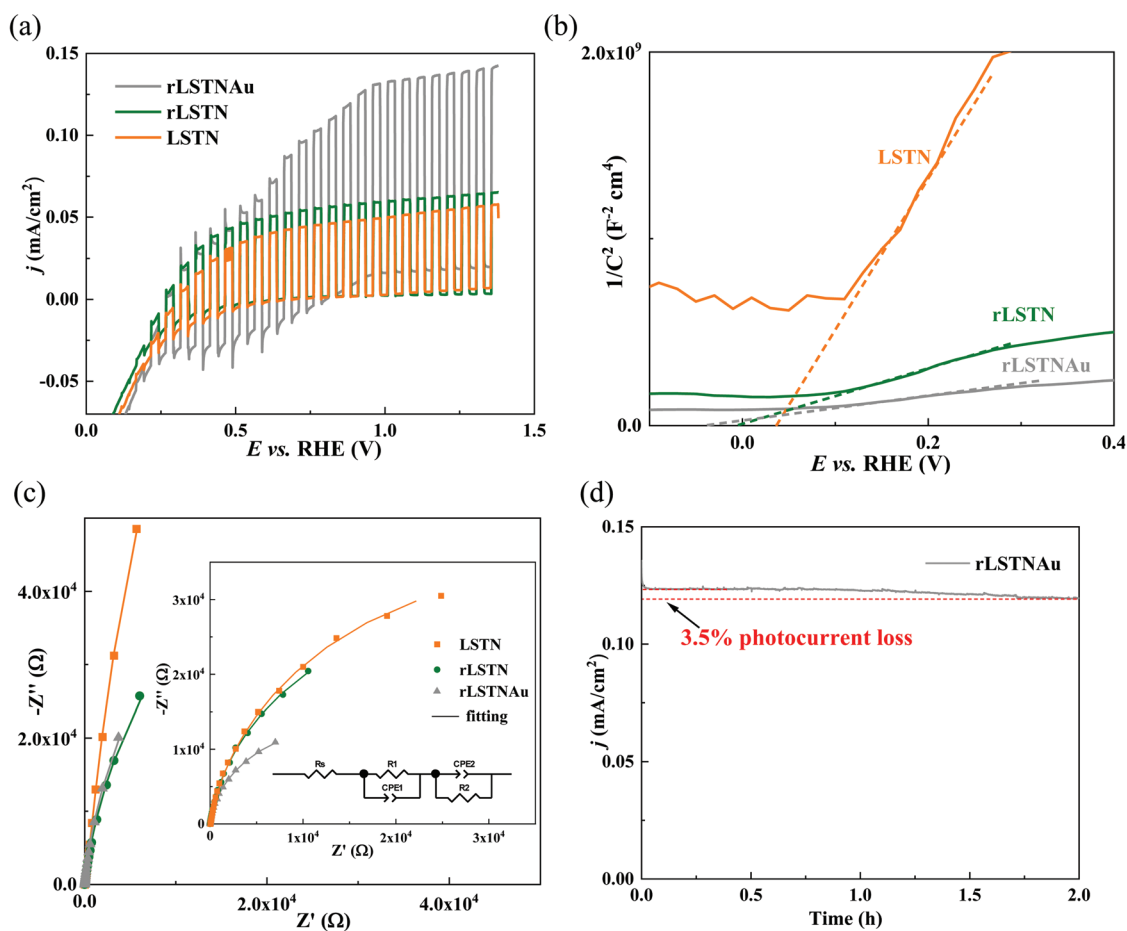
Figure 3. Real time observations via in situ STEM of the temperature-dependent NiAu NPs reconstruction on the perovskite surface. Au has a higher atomic number than Ni and appears brighter in the STEM-DF mode. A series of STEM DF frames and the corresponding EDS maps of the selected NiAu particles on the rLSTN surface with different temperatures are given. The temperature ramp rate was ≈100 °C s^{-1}, and the snapshots were taken after staying after equilibrating at the specific temperatures for a few seconds. Yellow, Au; cyan, and Ni.

2.3. Photoelectrochemical Activity of Post-Annealed rLSTNAu

We studied the PEC water electrolysis performance of the supported NiAu system in 1 M KOH electrolyte under simulated 1 sun illumination and compared it against the LSTN and rLSTN samples. A set of linear sweep voltammograms (LSVs) were recorded, as shown in **Figure 4**a. The photocurrent response during intermittent illumination of constant intervals was spike-free, especially at applied potential >0.5 versus reversible hydrogen electrode (RHE), indicating a good charges carriers separation efficiency in all the samples. On the other hand, the photocurrent density of the rLSTNAu sample (containing both the mixed flower-like and antenna–reactor-like structures) reached 140 mA cm^{-2} at 1.23 V (vs RHE), which is 2.2 and 2.5 times, higher than in the LSTN and rLSTN samples, respectively. To compare the activity of rLSTN and LSTN, we

repeated the LSV tests several times with electrodes made in different batches. Statistically, we observed that the improvement of charge current is not obvious after Ni exsolution, which means Ni alone has limited efficacy toward PEC water splitting. The intrinsic defects induced during the reduction process of rLSTN are likely becoming trapping centers for charge annihilation, which may also undermine photocatalytic activities.[21] On the other hand, our novel and facile introduction of Au greatly improved the PEC performance.

We conducted additional PEC measurements in order to further investigate the semiconducting properties of the samples and the interfacial electrochemistry during photoelectrocatalytic testing. Mott–Schottky (M–S) measurements were employed to study the basic mechanism behind the increase in photocurrent density, considering that the slope in the M–S plot is inversely proportional to the donor concentration (N_D) in the

**ADVANCED
SCIENCE NEWS**

www.advancedsciencenews.com

NANO · MICRO

small

www.small-journal.com

Figure 4. PEC performance of LSTN, rLSTN and rLSTNAu. a) Linear-sweep voltammograms from 0–1.38 V (vs RHE), b) Mott-Schottky plots obtained at 1000 Hz, c) Nyquist plots under dark and illumination (inset) conditions at a bias potential of 1.23 V (vs RHE) under a frequency range from 10^5 to 0.1 Hz with an amplitude of 10 mV. The inset shows also the equivalent circuit used to fit the raw data. d) The chronoamperometric test under 1 sun illumination at 1.23 V (vs RHE) for 2 h.

semiconductor, and the intercept reflects the flat band potential (V_{fb}).[22] M–S plots in Figure 4b indicate the n-type conductivity of the as-prepared samples with a positive slope and an S-shape of the curves. Table S1 (Supporting Information) summarizes the slopes and intercept values from the M–S plots. The results show that the donor concentration increased significantly after Ni exsolution (decreasing slope values), which means the electronic properties of the LSTN semiconductor are efficiently improved. The addition of Au further increased the donor density, accompanied by a slight shift of the flat band potential to more negative values (from 60 to −70 mV vs RHE). This means that the Fermi level (E_F) is slightly shifted to more negative energy levels by reduction and exsolution, as well as subsequent Au deposition, altering the intrinsic energy levels of the semiconducting substrate. Together with the plasmonic activity and the improved charge separation in the flower- and antenna–reactor-like structures the PEC performance is enhanced.

To further study and understand the interfacial PEC reaction kinetics and the charge carriers' separation efficiency, electrochemical impedance spectroscopy (EIS) and incident-photon-to-current-efficiency (IPCE) measurements were conducted

at an applied potential of 1.23 V versus RHE under dark and illuminated conditions. IPCE measurements given in Figure S9 (Supporting Information) clearly show that the highest IPCE along the whole spectrum range was achieved on the rLSTNAu photoanode. EIS measurements represented by the Nyquist plots of Figure 4c, indicate that the low frequency resistances are much larger in dark conditions than under illumination, representative of slow or even blocking electrode process kinetics.[23] Upon illumination, the low frequency resistances for rLSTN with Ni exsolution is smaller than that of pristine LSTN photoanode, while rLSTNAu shows the smallest resistance (see Table S1, Supporting Information) for the deconvoluted resistance and capacitance data). Therefore, the supported NiAu bimetallic structure possesses the strongest separation efficiency of electron-hole pairs, which is a key factor for high PEC performance. This is also assessed in terms of stability under potentiostatic conditions in strongly alkaline media. As it is seen in Figure 4d, the photocurrent retains 97% of its initial value after 2 h of constant illumination. We performed an additional stability testing and as shown in Figure S10 (Supporting Information), a 10% degradation is observed after 24 h of constant illumination, increasing to 33% after 48 h. These

ADVANCED
SCIENCE NEWS
www.advancedsciencenews.com

NANO · MICRO
small
www.small-journal.com

results indicate a very promising stability of the supported NiAu bimetallic photoanode under strongly alkaline conditions, but further studies are needed to elucidate the degradation mechanism.

3. Mechanistic Insights and Shift in Catalytic Activity

3.1. Structure-Plasmonic Property Correlations

To provide mechanistic insights in the superior PEC performance of the galvanically restructured rLSTN, the plasmonic behavior of the supported NiAu system in the antenna–reactor-like and flower-like structures (will be referred to as "configurations" in the simulations) was studied. Electron energy loss spectroscopy (EELS) was employed and complemented by both Metal NanoParticle Boundary Element Method (MNPBEM) and Finite Difference Time Domain (FDTD) simulations as displayed in **Figure 5**. The dielectric constant of La-doped SrTiO$_3$ (LSTO), as found by Duan et al. for La$_{0.625}$Sr$_{0.375}$TiO$_3$,[24] was used in the simulations under the assumption that after Ni exsolution, our substrate, LSTN, is close to LSTO.

The HAADF image and the EDS mapping of Figure 5a depict one Au nanoparticle with a diameter of 21 nm adjacent to a Ni nanoparticle of 16 nm in diameter, a unique configuration considered as antenna–reactor.[6,25] Their relative position on the LSTN particle is given in Figure 5a, together with the region that the EELS spectra were recorded (Figure 5b,c). We observe a prominent excitation from the Au NP (antenna), especially at ≈2.4 eV in the region around the Au NP, but also around the adjacent Ni NP (reactor), as well as between them. This is more evident when looking at the color maps, which represent the number of electrons having lost energy between 2.38 and 2.40 eV, and 2.40 and 2.42 eV, respectively (Figure 5c and Video S1, Supporting Information of EELS spectrum with energies between 1.40 and 4.00 eV).

Figure 5d shows the simulated loss probability (P_{loss}) map of a Au NP on an LSTO NP at energies close to the LSPR energy of Au in vacuum. The highest loss in the simulated map is found at the edge of the Au NP pointing away from LSTO. This is similar to what the experimental EELS map shows. Furthermore, Figure 5e shows the P_{loss} map of a Ni and Au NPs touching at 1.85 eV and not touching at 2.4 eV. Most of the loss is clearly around the Au NP at 2.4 eV, while for the touching case, there is an additional mode at 1.85 eV which has the highest loss at the part of the particle diametrically opposite from their intersect. The average simulated P_{loss} spectra in 5f, from the areas marked in 5e, show an LSPR peak in both the Au and the Ni NPs at the Au's LSPR energy (2.4 eV) for both the touching case and the not touching case. The peak at 2.4 eV in the Ni NP in both simulations and the measured EELS spectra indicate that the energy absorption of the Ni nanoparticle is enhanced due to the adjacent Au NP. The absence of gap between the particles does not seem to change the absorption in Ni due to the main Au plasmon peak at 2.4 eV. The appearance of the extra peak at 1.85 eV was investigated with additional simulations and its energy was found to be dependent on the amount of overlap between the particles. In Figure S11 (Supporting Information)

the peak is shifted between 1.65 and 2.00 eV, indicating that a small change in the particles' overlap will shift the peak energy significantly.

Additional simulations confirm the antenna–reactor effect due to the electromagnetic coupling effect between Au and Ni NPs.[26] An increase in absorption is present both for a Ni NPs in water and surrounded by water but embedded on LSTO (Figure 5g,h), a configuration that closely resembles the PEC experiments. The absorption of the Ni reactor increases with increasing Au size and decreasing inter-particle distance (Figures S12 and S13, Supporting Information). Moreover, we observe that the absorption in the Au NP is also increased by the presence of the Ni NP (Figure 5i). It seems that the presence of the Ni NP can compensate for the lower absorption when Au is embedded on LSTO compared to only surrounded by water. A possible explanation for the lower Au absorption when embedded in LSTO is that an energy transfer occurs from the excited Au NPs to the immediate surroundings of LSTO, visualized as a broadening and lowering of the LSPR peak. Although the Ni NPs are expected to have a NiO$_x$ shell (refer to Figure S8, Supporting Information), especially under anodic PEC water splitting conditions, FDTD simulations still indicate a strong antenna–reactor effect of Au on a core-shell Ni-NiO NP (Figure S12, Supporting Information). Interestingly, we see that the absorption cross section of the Ni NP with an oxide layer is larger than a Ni NP without an oxide layer, here shown for the extreme case with an oxide thickness of 3 nm.

In the flower-like configuration, which is expected to contribute to the PEC performance in synergy with the antenna–reactor one, Au NPs grow around the Ni particle with some of the Au NPs being in direct contact with Ni (Figure S4, Supporting Information). Therefore, FDTD simulations were done for Ni NPs that are surrounded by a random number of Au NPs of different sizes, in accordance with the SEM and STEM observations (Figure 2; Figures S4–S7, Supporting Information). In a hypothetical situation where the Ni NPs are removed, the simulations indicate that the absorption is higher and the Q-factor is larger than that in the presence of Ni NPs (Figure S14, Supporting Information) but the difference is small. Although any antenna–reactor effects are not expected due to electron tunneling,[26] we did see electron energy losses in the Ni NPs earlier at ≈1.85 and 2.40 eV (simulations), but also in the EELS spectra (experimental data) in Figure S15 (Supporting Information) and corresponding EELS (Video S1, Supporting Information). Based on these experimental evidences we can conclude that the charge transfer between the two metals does not completely hinder absorption in either NP. A similar system where the antenna NPs/single atoms are in contact with the reactor have been reported by Zhou et al., in a CuRu, antenna(Cu)–reactor(Ru) system.[6a] More importantly, our calculations in Figure S14e–g (Supporting Information) show that the electric field is boosted when Au NPs approach each other as compared to isolated ones. Therefore, the plasmonic flower-like and antenna–reactor hybrid structures, which can now be facilely realized and further developed through our reported methodology, can produce more effective photocatalysts than singly supported plasmonic NPs.

To complement our EELS and simulation studies with additional experimental evidence, we conducted diffuse-reflectance
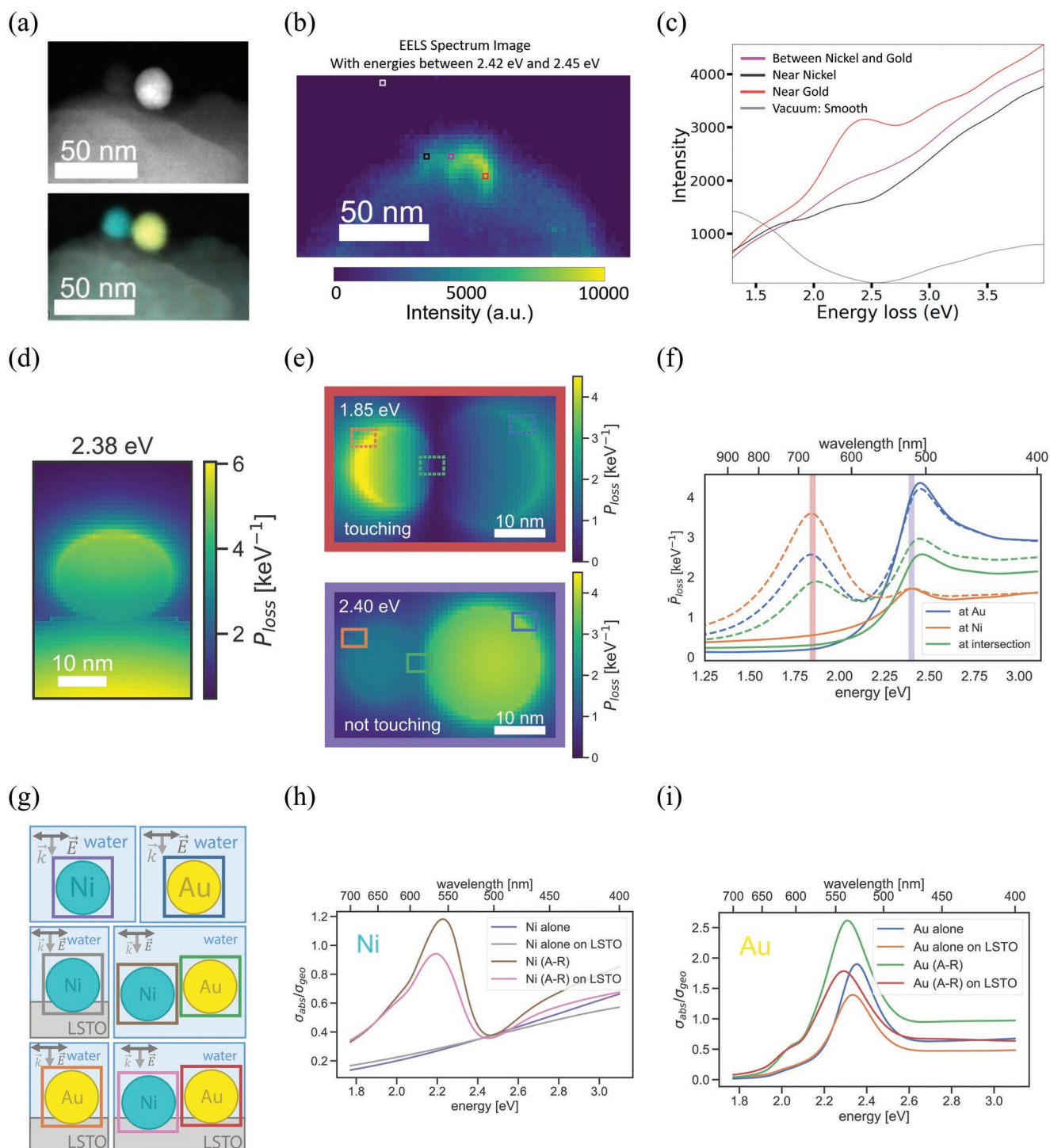
Figure 5. EELS and MNPBEM and FDTD simulations. a) HAADF-STEM and the corresponding EDS image of rLSTNAu in a bimetallic antenna–reactor-like configuration. b) EELS map at energy of Au LSPR mode, i.e., ≈2.4 eV. c) EELS spectral components of the specific antenna–reactor configuration at positions shown in (b). Simulated loss probability maps of d) Au on LSTO NP (diameter 100 nm) near LSPR energy and e) simulated loss map of Ni NP (left) and Au NP (right) touching (i.e., the Au NP is pertruding into the Ni NP) at 1.85 eV and with a small gap (1 nm) at 2.40 eV. f) Simulated loss probability spectra at positions marked in (e), the touching case (dashed lines) and the not touching case (solid lines). g) Different configurations used to calculate absorption cross-sections of example antenna–reactor. The absorption cross-sections normalized by the geometrical cross-section for Ni and Au NPs in different situations are shown in h) and i), respectively.

spectroscopy (DRS), steady-state photoluminescence (PL), and time-resolved photoluminescence (TRPL) measurements (**Figure 6**).

The differential DRS spectra of Figure 6a show the increased extinction in the visible region with maximum at ≈2.4 eV, a direct
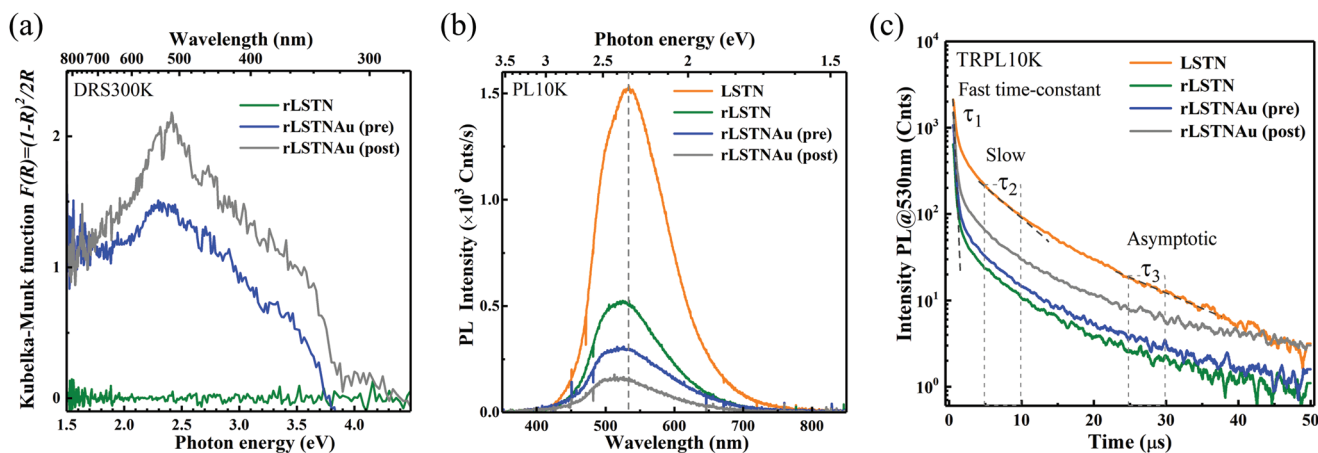
Figure 6. Optical absorption and emission properties of LSTN, rLSTN, rLSTNAu (pre annealed) and post-annealed rLSTNAu. a) Kubelka–Munk function (absorbance) derived from differential diffuse-reflectance with reference to rLSTN ($R_{diff} = R_\# / R_{rLSTN}$), b) steady-state PL emission spectra obtained at 10 K, c) TRPL transients revealing non-exponential dynamics of the photo-excited carrier recombination ascribed by three decay time constants.
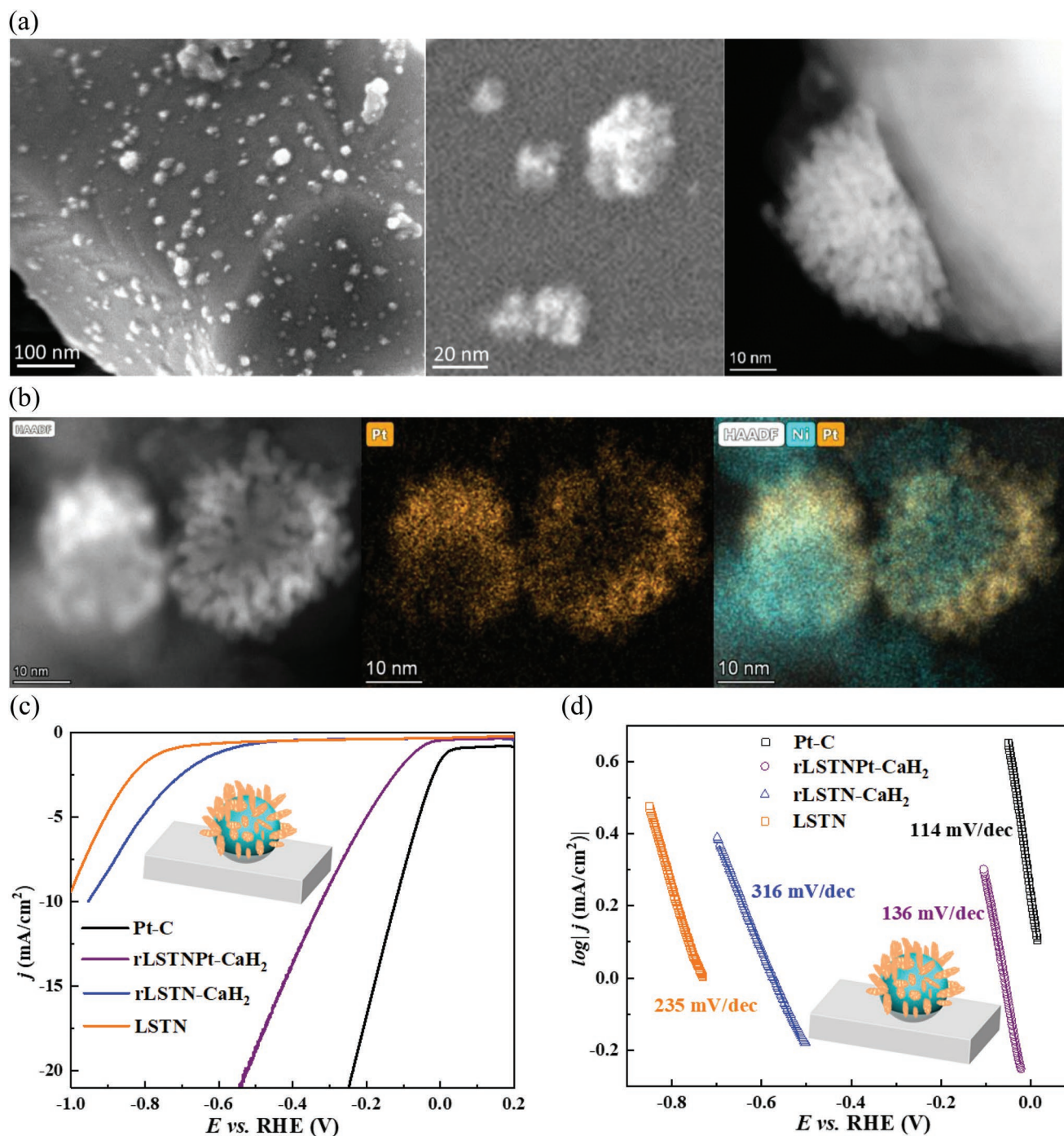
proof of plasmonic effect due to Au incorporation that appears further enhanced by postannealing. The results are consistent with the fact that excitation of LSPR in Au NPs results in an extreme concentration of light and an enhanced electric field around the nanostructures, leading to the significant enhancement in absorption and scattering efficiencies for photons at the resonant energy.[27] As our experimental particle structures have a large variety of overlapping between the particles, as well as sizes, we do not expect to see a distinct peak at 1.85 eV in measurements like PL or DRS. Instead, the differently overlapping particles might result in a broad peak or shoulder in the region ≈1.6 to 2.0 eV, but we do not see such evidence clearly. This could be attributed to a) increased overlap between Ni and Au NPs and/or b) increasing ratio between the radius of Ni and Au NPs (Figure S11, Supporting Information), red-shifting their peak energy. On the other hand, the magnitude of each contribution is currently unknown and necessitates further studies. The steady-state PL spectra in Figure 6b show that the Au incorporation leads to significant decrease of the quantum efficiency as compared to LSTN. The likely cause of the quenched PL is that the photoexcited electrons from the conduction band of LSTN are being transferred of to the Fermi level of the Au NPs, the plasmonic absorption region of which overlaps with that of LSTN emission. The dynamics of this mechanism is elucidated by the TRPL measurements (Figure 6c). The shortest lifetime (τ_1) observed for rLSTN-Au (Table S4, Supporting Information) might be associated either with extra non-radiative pathway due to deterioration of crystallinity upon Au incorporation (which is unlikely according to the XRD analyses), or to plasmonic effect leading to LSPR-enhanced charge transfer between the Au NPs and LSTN. More information and additional DRS and TRPL results can be found in Note S2, Figures S26 and S27 and Table S4 (Supporting Information).

3.2. Shift of Catalytic Activity to Hydrogen Evolution Reaction with NiPt Bimetallic NPs

In order to generalize our method, we galvanically hybridized Ni NPs with platinum (Pt) through the GRR method for

the synthesis of a hydrogen evolving catalyst. We remind that in this case a highly conducting substrate material is desired, therefore the reduction of LSTN was done in the presence of CaH_2 (refer to experimental and electrochemical activity of rLSTNPt part in Figures S16–S23, Supporting Information). Impedance measurements confirm that the conductivity of the reduced LSTN by CaH_2 (rLSTN-CaH_2) is greatly improved compared to the LSTN, as well as rLSTN (Figure S17, Supporting Information). As displayed by the SEM, HAADF-STEM, and EDS analyses of **Figure 7**a,b, Pt deposits grow on the Ni NPs with a morphology similar to a hedgehog-like structure. It is noted that the rLSTN-Pt sample shows also a hedgehog-like structure as seen in Figure S18 (Supporting Information). Compared to our plasmonic NiAu structures, the lattice mismatch of Ni and Pt is smaller (≈11%), with a less significant difference in electronegativity and atomic radius, which results in a narrowed miscibility gap. Therefore, unlike Au that tends to form isolated NPs, Pt is more likely to grow around the Ni NPs, and the inter-diffusion of Ni and Pt atoms at their interface should happen easier. The obtained hybrid NiPt hedgehog-like structure shows an exceptional improvement of the electrochemical performance of the rLSTNPt sample for the HER in 0.1 M KOH. An overpotential of −320 mV versus RHE at 10 mA cm^{-2} represents a high electrocatalytic activity toward the HER approaching that of the state-of-art and commercial Pt-C HER catalyst. The Tafel slope of 135 mV dec^{-1} indicates the Volmer reaction as the rate determining step, which is also the case for the Pt-C with a Tafel slope of 114 mV dec^{-1}. The superior performance of the Pt-C is attributed to the much higher Pt content and superior conductivity of carbon. The peak in the underpotential deposition region of hydrogen atoms (UPD-H) was used in acidic conditions (0.1 M $HClO_4$),[28] and the estimated electrochemically active surface area (ECSA) of Pt-C is ≈1.2 cm^2, while for rLSTNPt-CaH_2 is only ≈0.03 cm^2, that can be directly correlated to a significantly lower Pt amount (factor of 40) in the rLSTNPt-CaH_2.

To further support this, we estimated the double layer capacitance, which is a direct measure of the ECSA, in the non-faradaic region by cyclic voltammetry (CV) and impedance

ADVANCED
SCIENCE NEWS
www.advancedsciencenews.com

NANO · MICRO
small
www.small-journal.com

(a)

(b)

(c)

(d)

Figure 7. Structural observations and electrochemical performance of Pt-nano-engineered LSTN. a) SEM images of rLSTN-CaH$_2$ after reduction with CaH$_2$ at 600 °C, showing the exsolved Ni NPs. b) HAADF-STEM images and EDS maps of rLSTNPt-CaH$_2$ after galvanic replacement with PtCl$_6^-$ in 0.1 M HClO$_4$, revealing the coexistence of Ni and Pt in a hedgehog-like morphology. c) LSV curves and d) Tafel slopes of the perovskite-based samples and the commercial Pt-C electrocatalyst. The potential scanning rate was 10 mV s^{-1} in 0.1 M KOH electrolyte.

spectroscopy. Table S3 (Supporting Information) shows that both methods give the same trends in double layer capacitances between the LSTN-based and Pt-C samples. Notably, a factor of ≈24 by the CV method indicates again the much larger ECSA of the Pt-C, which can also be seen in its nanostructure (Figure S24, Supporting Information). Finally, rLSTNPt-CaH$_2$

shows good stability under galvanostatic operation at −10 mA cm^{-2}, and a 20% increase in the overpotential is seen after 48 h of operation in 0.1 M KOH (Figure S25, Supporting Information). A partial loss of powder from the carbon support is also responsible for the overpotential increase and apparent instability of the material.

**ADVANCED
SCIENCE NEWS**

www.advancedsciencenews.com

**NANO · MICRO
small**

www.small-journal.com

4. Conclusions

This work introduces a new method to prepare functional bimetallic hybrid nanostructures supported on perovskite surfaces, such as on $SrTiO_3$, with minimal engineering and high catalytic versatility. In situ metal exsolution followed by galvanic replacement and deposition can easily stir the catalytic activity from plasmonic photocatalysis (NiAu NPs supported on LSTN) to hydrogen evolving cathodes (NiPt NPs supported on LSTN), by merely deciding on composition of the galvanic replacement solution. Our approach opens up tremendous opportunities in the synthesis of well-adhered and supported bi- or multi-metallic, catalytically active NPs of improved activity and tunable properties and structures. Optimization of the different synthesis parameters will further improve the control for targeted hybrid structures, like core-shell, antenna–reactor, and multi-metallic alloys with the desired catalytic properties beyond water splitting through minimal engineering and amounts of both precious and non-critical elements.

5. Experimental Section

Synthesis of Supported Ni-Based Bimetallic Catalysts: The samples were synthesized by a modified solid-state route using high purity precursors, including $Ni(NO_3)_2 \cdot 6H_2O$, La_2O_3 (dried at 800 °C), $SrCO_3$, and TiO_2 (both dried at 300 °C). The dried powders were weighed while hot (nickel nitrate was cold) in the appropriate stoichiometric ratios for the composition $La_{0.6}Sr_{0.2}Ti_{0.9}Ni_{0.1}O_{3-x}$ and mixed in a beaker with acetone. The mixture underwent ultrasonic treatment to break down agglomerates. The acetone was evaporated under continuous stirring to ensure further homogenization, and then the powder was pressed into a pellet and calcined at 1000 °C for 12 h. The calcined powder was crushed and ball-milled for 2 h at 250 rpm, and then pressed into a pellet again for the second sintering at 1100 °C for 12 h. The final perovskite powders were prepared by repeating the above step for the third time calcination at 1200 °C for 10 h.

The exsolution process was carried out in a ProboStat cell (NORECS, Norway) under continuous pure H_2 gas flow at atmospheric pressure and calcined at various temperatures, the resulting sample was donated as rLSTN. The Ni exsolution was also achieved for the first time by mixing LSTN powder and CaH_2 in a molar ratio of 1:3 (rLSTN-CaH_2). Then the mixture was pelletized and put in an ampoule, which was sealed under vacuum ($<5.0 \times 10^{-2}$ bar). The sample was heated at 600 °C for 3 days, and then washed in methanol containing 0.1 M NH_4Cl to remove the CaO and the excess CaH_2.

The bimetallic nanostructures were prepared via a facile galvanic replacement reaction. Typically, the freshly prepared exchange solution containing 2.5 mL gold ion precursor (1×10^{-3} M HCl + 1×10^{-3} M $HAuCl_4$, pH = 3) and 1 mL PVP (1×10^{-3} M) was deaerated by N_2 bubbling for 20 min at 80 °C. Then, the as-synthesized rLSTN powders were dispersed into the solution, during which the spontaneous Ni dissolution and Au deposition occurred:

$$3Ni + 2AuCl_4^- \rightarrow 2Au + 3Ni^{2+} + 8Cl^- \qquad (1)$$

The standard chemical potential of $AuCl_4^-$ ($E^0(AuCl_4^-/Au) = 1.002$ V vs the standard hydrogen electrode (SHE)) was much higher than Ni ($E^0(Ni^{2+}/Ni) = -0.257$ V vs SHE), rendering a very fast replacement. The reaction lasted for only 1 min, and was quenched immediately by cold deionized water. The final powders (rLSTNAu) were collected and washed with deionized water. The removal of oxygen and a moderate acidic atmosphere during replacement reaction were crucial for efficient and fast noble metal deposition, avoiding the more favorable oxygen reduction reaction ($E^0(O_2/H_2O) = 1.23$ V vs SHE) or even the possible

competitive hydrogen evolution reaction ($E^0(H^+/H_2) = 0$ V vs SHE). The elevated temperature and a short reaction period not only enhanced the reaction kinetics, but also ensured the decoration of those tiny Au nanocrystals on the Ni surface instead of aggregating.

In order to obtain rLSTNPt-CaH_2 from rLSTN-CaH_2 powders, the $HAuCl_4$ solution was replaced with a H_2PtCl_6 solution. Considering the different standard chemical potentials,

$$E^0(PtCl_6^{2-}/Pt) = 0.744 \text{ V vs SHE} \qquad (2)$$

the time was adjusted to 5 min to ensure a sufficient reaction.

Characterizations: The phase purity and crystal structure of the prepared perovskites as well as bimetallic nanostructures were confirmed by room temperature X-ray diffraction (XRD, Bruker D8 Discover, Cu $K_{\alpha 1}$, Bragg-Brentano). Si powders were used to correct the instrumental peak-shifting. Rietveld refinement analysis was conducted using Topas software. The following parameters were gradually unlocked and refined: background (Chebyshev coefficient, 5–9 terms), peak shape, unit cell parameters, atomic coordinates, site occupancies, thermal displacement parameters, and microstrain. The pseudocubic perovskite cell parameter a_p (A) was calculated as: $a_p = \sqrt[3]{\frac{V}{4}}$, where V is the volume of the perovskite unit cell calculated from Rietveld refinement. Scanning electron microscopy (SEM, Hitachi SU8230 ultra-high resolution cold-field emission SEM equipped with a secondary electron (SE) detector under an acceleration voltage of 5 kV) was used to image the series of nanostructures, calculating the particle size distribution and population. As the ladybug structure was metastable and quickly evolved to the flower-like (see Section 2.1), SEM for the ladybug was done right after the high temperature reduction process.

STEM and high-resolution EELS were performed using an FEI Titan G2 60–300 instrument. The instrument was equipped with a CEOS DCOR corrector for the probe forming lenses, a Wien-filter monochromator, a Gatan 965 Quantum EELS spectrometer, and the FEI Super-X EDS detector. For structural and chemical characterization, the instrument was operated at an accelerating voltage of 300 kV, with a probe convergence semi-angle of 21 mrad. The inner collection semi-angle was 101, 22, and 9 mrad for the HAADF, DF4, and DF2 detector, respectively. Surface plasmon mapping was done at 60 kV with an energy resolution of ≈110 meV as measured using the full-width-half-maximum (FWHM) of the zero loss peak. In situ heating experiments were performed using the Protochips Fusion 350 double-tilt sample stage. The stage utilizes resistive ceramic heating chips, each individually calibrated by the manufacturer to an accuracy of better than 5%. A stability better than 0.01 °C is guaranteed by the manufacturer. The temperature uniformity across the viewing area of the chip is better than 99.5%, and the displacement after a temperature ramp of 325 °C was <7 nm, with an ultimate drift rate of 0.5 nm min^{-1}. It is important to note that all the specifications were stated by the manufacturer, and were not individually verified.

The EELS maps were analyzed using a custom made Python code, utilizing the hyperspy package.[29] The zero-loss peaks were aligned to 0 eV, and the energy resolution determined by measuring the FWHM. Subsequently, the background was subtracted for each individual plot, fitted to a suitable energy range. A Gaussian filter with a width matching the energy resolution was used to deconvolute the spectra further. To visualize the peaks in the energy loss spectra for all pixels, an integration was performed over a tiny energy range. This range was set to three times the energy resolution. The integrated values were plotted as contour plot using the matplotlib library,[30] and the videos (Videos S1 and S2, Supporting Information) were made by combining the individual frames. Moreover, individual spectra from marked pixels were plotted.

The optical absorption properties were investigated at room temperature by means of DRS using EVO-600 (Thermo Fisher Scientific, Inc.) UV–Vis spectrophotometer. The emission properties were attained by steady-state PL measurements carried out at 10 K in a CCS450 (Janis Research Company, LLC) closed-cycle He refrigerator system and using a 325 nm wavelength He–Cd cw-laser as an excitation source

ADVANCED
SCIENCE NEWS
www.advancedsciencenews.com

NANO · MICRO
small
www.small-journal.com

(power density <10 W cm^{-2}). The luminescence was collected by a microscope and analyzed by USB4000 (Ocean Optics, Inc.) fiber-optic spectrometer with a spectral resolution below 2 nm. The recombination and trapping dynamics of the photo-excited carriers were assessed by TRPL measurements performed at 10 K by employing 372 nm wavelength ps-laser (PicoQuant LDH375, 50 ps-pulsed 2mW @40MHz) as an excitation source. The selected spectral region was filtered out from the total PL signal using imaging spectrograph (HORIBA Jobin Yvon, iHR320) and registered by photon counting system (PicoQuant NanoHarp250, Becker&Hickl PMC100).

Catalyst Performance Evaluation: PEC measurements were performed on a standard three-electrode set up with NaOH (1 м, pH 13.6) as the electrolyte, Hg/HgO and a platinum foil as the reference electrode and counter electrode, respectively. The working electrodes containing the investigated catalysts were prepared as follows: adding 100 mg of powder in a mixture of 2.5 mL water, 1.25 mL isopropanol, and 30 µL of 5 wt.% Nafion, followed by the sonication for 3 h to obtain a homogeneous ink. Applying 50 µL of ink on the Ti foil (1 cm^2) by the drop-cast method and then anneal at 600 °C under an inert atmosphere for 0.5 h to achieve the stable reconstructed nanostructure, in addition to a better adhesion with the Ti foil substrate. All the tests were conducted by a Gamry Reference 3000 potentiostat, under 1 sun simulated solar light from a Newport Oriel LCS-100 solar simulator equipped with a 100 W ozone-free xenon lamp and an AM 1.5G filter. The light intensity was regularly calibrated by a monocrystalline Si PV reference cell (Newport 91150V-KG5). All over potentials are corrected against the RHE taking into account that water electrolysis takes place thermodynamically at 1.23 V versus RHE. Therefore, the potentials were corrected versus RHE according to the Nernst Equation:

$$E_{RHE} = E_{meas.} + 0.059 \text{ V} \times pH + 0.121 \text{ V} \qquad (3)$$

Photocurrent at the applied bias of 1.23 V vs RHE was measured as a function of wavelength for the calculation of IPCE with the following equation:

$$IPCE = \frac{j_p 1240}{\lambda I_0} \qquad (4)$$

where j_p is the photocurrent density (mA cm^{-2}), λ is wavelength of the incident light in nm, and I_0 is the wavelength dependent intensity of incident light (mW cm^{-2}).

The electrochemical measurements were also carried out following a similar procedure with the above PEC test. A rotating disc electrode (RDE) with glassy carbon (GC) as the tip (RDE710 Rotating Electrode from Gamry Instruments) was used as the working electrode, a standard Hg/HgO as the reference and a graphite rod as the counter electrodes. The supporting electrolyte was 0.1 м aqueous KOH solution. The RDE was coated with the as-prepared catalyst ink according to the procedure suggested by S. Jung et al.[31] The inks were drop-cast on the GC tip (0.196 cm^2) by applying 4 µL of ink and then dried for 10 min at 60 °C. This procedure resulted in the loading of ≈0.5 mg of the electrocatalyst on the GC. For long-term stability experiments, the same amount of powder (≈0.5 mg) was loaded by drop-casting on C paper of a nominal surface area of 1 cm^2 with a mass loading of 0.5 mg cm^{-2}.

Simulation Details: The simulations of surface plasmons excited by a light source were performed with Ansys Lumerical's FDTD software, which uses the FDTD method to solve Maxwell's equations. The source used was the Total field/Scattered field (TSFS) source and the absorption was calculated using the frequency-domain field and power monitors. The monitors were placed as indicated in the illustration in Figure 5g. The electric field of the plane wave source was parallel to the surface of LSTO and pointing from one NP to the other in the cases with two NPs. The simulation region was meshed using a nonuniform mesh with a mesh size of 0.8 nm (A-R) and 0.75 nm (flower) within the TSFS source region. One simulation of the antenna–reactor configuration with mesh size 0.5 nm was tested and resulted in a peak height change of 3% for Ni and 1% for Au. This test-simulation gave an absorption peak

energy blue-shift for Ni of 0.02 eV, and for the Au absorption spectra, a small change in shape where the small peak at lower energies, ≈2 eV, became less prominent. The same test simulation was done for one of the flower-configurations which resulted in a 3% change in peak height and a less prominent peak at 2 eV. The rest of the region was meshed automatically with mesh accuracy 4. Conformal variant 0 was used and all boundaries were set to be absorbing using perfectly matched layers.

The simulations of surface plasmons excited by an electron beam source, i.e., the calculation of P_{loss}, were done using MNPBEM.[32] The simulations were performed with a retarded solver and using curved particle boundaries. The Au, Ni and LSTO NPs were made using the trispheresegment-function. In the antenna–reactor (A–R) configuration, the Ni (Au) sphere surface was discretized using 21 (32) mesh points for theta and 16 (24) for phi. While for the Au NP on a LSTO NP and the touching A–R configuration the amount of overlap between the NPs was defined with an overlap angle of 0.2 π and 0.1 π from the center of the Au NP, respectively (see Figure S11, Supporting Information for an overlap angle explanation). The surfaces of the spheres were discretized using 21 mesh points for theta and 16 for phi. The segment representing the boundary between the Au and the LSTO was defined with 16 mesh points for phi and 6 for theta. For the EELS simulations it had a beam size of 0.32 and a velocity that corresponded to 60 keV. The dielectric functions used for Au and Ni within FDTD was from Lumerical's database which has them from the CRC Handbook of Chemistry and Physics, and the one used for LSTO was extracted using WebPlotDigitalizer developed by Rohatgi.[24,33] The same dielectric function for LSTO was used within the MNPBEM simulations, but for Au and Ni dielectric functions from Johnson and Christy were used.[34]

Supporting Information

Supporting Information is available from the Wiley Online Library or from the author.

Acknowledgements

Conflict of Interest

The authors declare no conflict of interest.

Author Contributions

X.K. synthesized all materials, performed experiments and wrote the original draft. V.M.R. performed all calculations and contributed to writing, review, and editing. K.G.B. performed TEM and EELS measurements and analyses, did the color plots and particle size analyses and contributed to writing, review and editing. A.G. performed and analyzed all DRS and PL measurements. T.A. performed TEM and in situ TEM measurements. Ø.P. did supervision and contributed insights to TEM and EELS. T.N. did supervision, provided resources, and contributed to review and editing. D.N. provided insights and contributed to writing, review, and editing and A.C. conceptualized and supervised the work, did project management and administration, provided insights and contributed to writing, review, and editing.

Data Availability Statement

The data that support the findings of this study are available from the corresponding author upon reasonable request.

Keywords

[1] a) C. H. Wu, C. Liu, D. Su, H. L. Xin, H.-T. Fang, B. Eren, S. Zhang, C. B. Murray, M. B. Salmeron, *Nat. Catal.* **2019**, *2*, 78; b) N. Danilovic, R. Subbaraman, K. C. Chang, S. H. Chang, Y. Kang, J. Snyder, A. P. Paulikas, D. Strmcnik, Y. T. Kim, D. Myers, V. R. Stamenkovic, N. M. Markovic, *Angew. Chem. Int. Ed. Engl.* **2014**, *53*, 14016; c) X.-Z. Song, L. Qiao, K.-M. Sun, Z. Tan, W. Ma, X.-L. Kang, F.-F. Sun, T. Huang, X.-F. Wang, *Sens. Actuators, B* **2018**, *256*, 374.

[2] a) J. E. Bruno, N. S. Dwarica, T. N. Whittaker, E. R. Hand, C. S. Guzman, A. Dasgupta, Z. Chen, R. M. Rioux, B. D. Chandler, *ACS Catal.* **2020**, *10*, 2565; b) W. Zhan, J. Wang, H. Wang, J. Zhang, X. Liu, P. Zhang, M. Chi, Y. Guo, Y. Guo, G. Lu, S. Sun, S. Dai, H. Zhu, *J. Am. Chem. Soc.* **2017**, *139*, 8846; c) C. H. Wu, C. Liu, D. Su, H. L. Xin, H.-T. Fang, B. Eren, S. Zhang, C. B. Murray, M. B. Salmeron, *Nat. Catal.* **2018**, *2*, 78; d) J. Ahn, L. Zhang, D. Qin, *ChemNanoMat* **2019**, *6*, 5.

[3] Q. Zhang, J. Li, X. Liu, Q. Zhu, *Appl. Catal., A* **2000**, *197*, 221.

[4] a) R. Reichert, Z. Jusys, R. J. Behm, *J. Phys. Chem. C* **2015**, *119*, 24750; b) K. Awazu, M. Fujimaki, C. Rockstuhl, J. Tominaga, H. Murakami, Y. Ohki, N. Yoshida, T. Watanabe, *J. Am. Chem. Soc.* **2008**, *130*, 1676.

[5] S. Wang, Y. Gao, S. Miao, T. Liu, L. Mu, R. Li, F. Fan, C. Li, *J. Am. Chem. Soc.* **2017**, *139*, 11771.

[6] a) L. Zhou, J. M. P. Martirez, J. Finzel, C. Zhang, D. F. Swearer, S. Tian, H. Robatjazi, M. Lou, L. Dong, L. Henderson, P. Christopher, E. A. Carter, P. Nordlander, N. J. Halas, *Nat. Energy* **2020**, *5*, 61; b) D. F. Swearer, H. Zhao, L. Zhou, C. Zhang, H. Robatjazi, J. M. P. Martirez, C. M. Krauter, S. Yazdi, M. J. McClain, E. Ringe, E. A. Carter, P. Nordlander, N. J. Halas, *Proc. Natl. Acad. Sci. USA* **2016**, *113*, 8916.

[7] E. González, J. Arbiol, V. F. Puntes, *Science* **2011**, *334*, 1377.

[8] a) G. G. Li, Z. Wang, H. Wang, *ChemNanoMat* **2020**, *6*, 998; b) X. Xia, Y. Wang, A. Ruditskiy, Y. Xia, *Adv. Mater.* **2013**, *25*, 6313.

[9] A. Papaderakis, N. Pliatsikas, C. Prochaska, G. Vourlias, P. Patsalas, D. Tsiplakides, S. Balomenou, S. Sotiropoulos, *J. Phys. Chem. C* **2016**, *120*, 19995.

[10] D. Neagu, G. Tsekouras, D. N. Miller, H. Menard, J. T. Irvine, *Nat. Chem.* **2013**, *5*, 916.

[11] a) A. G. M. da Silva, T. S. Rodrigues, S. J. Haigh, P. H. C. Camargo, *Chem. Commun.* **2017**, *53*, 7135; b) J. Zhang, M.-R. Gao, J.-L. Luo,

Chem. Mater. **2020**, *32*, 5424; c) J. H. Kim, J. K. Kim, J. Liu, A. Curcio, J. S. Jang, I. D. Kim, F. Ciucci, W. Jung, *ACS Nano* **2021**, *15*, 81.

[12] X. Liu, P. Carvalho, M. N. Getz, T. Norby, A. Chatzitakis, *J. Phys. Chem. C* **2019**, *123*, 21931.

[13] S. Krishnamurthy, A. Esterle, N. C. Sharma, S. V. Sahi, *Nanoscale Res. Lett.* **2014**, *9*, 627.

[14] G. Tsekouras, D. Neagu, J. T. S. Irvine, *Energy Environ. Sci.* **2013**, *6*, 256.

[15] K. Kousi, D. Neagu, L. Bekris, E. I. Papaioannou, I. S. Metcalfe, *Angew. Chem.* **2020**, *132*, 2531.

[16] S.-B. Duan, R.-M. Wang, *Rare Met.* **2016**, *36*, 229.

[17] C. R. Stilhano Vilas, Boas, J. M. Sturm, W. T. E. van den Beld, F. Bijkerk, *Materialia* **2021**, *20*, 101203.

[18] A. Touni, X. Liu, X. Kang, P. A. Carvalho, S. Diplas, K. G. Both, S. Sotiropoulos, A. Chatzitakis, *ChemSusChem* **2021**, *14*, 4993.

[19] C. Cai, S. Han, W. Liu, K. Sun, L. Qiao, S. Li, X. Zu, *Appl. Catal., B* **2020**, *260*.

[20] a) S. Zhou, H. Yin, V. Schwartz, Z. Wu, D. Mullins, B. Eichhorn, S. H. Overbury, S. Dai, *ChemPhysChem* **2008**, *9*, 2475; b) H. Nishikawa, D. Kawamoto, Y. Yamamoto, T. Ishida, H. Ohashi, T. Akita, T. Honma, H. Oji, Y. Kobayashi, A. Hamasaki, T. Yokoyama, M. Tokunaga, *J. Catal.* **2013**, *307*, 254; c) M. Schnedlitz, M. Lasserus, R. Meyer, D. Knez, F. Hofer, W. E. Ernst, A. W. Hauser, *Chem. Mater.* **2018**, *30*, 1113; d) G. Zhao, J. Huang, Z. Jiang, S. Zhang, L. Chen, Y. Lu, *Appl. Catal., B* **2013**, *140–141*, 249.

[21] B. Liu, X. Zhao, J. Yu, I. P. Parkin, A. Fujishima, K. Nakata, *J. Photochem. Photobiol., C* **2019**, *39*, 1.

[22] a) M. Tayebi, A. Tayyebi, B.-K. Lee, *Catal. Today* **2019**, *328*, 35; b) C. Fleischer, A. Chatzitakis, T. Norby, *Mater. Sci. Semicond. Process.* **2018**, *88*, 186.

[23] T. Lopes, L. Andrade, H. A. Ribeiro, A. Mendes, *Int. J. Hydrogen Energy* **2010**, *35*, 11601.

[24] Y. Duan, P. Ohodnicki, B. Chorpening, G. Hackett, *J. Solid State Chem.* **2017**, *256*, 239.

[25] C. Zhang, H. Zhao, L. Zhou, A. E. Schlather, L. Dong, M. J. McClain, D. F. Swearer, P. Nordlander, N. J. Halas, *Nano Lett.* **2016**, *16*, 6677.

[26] K. Sytwu, M. Vadai, J. A. Dionne, *Adv Phys X* **2019**, *4*, 1619480.

[27] F. Wang, Y. R. Shen, *Phys. Rev. Lett.* **2006**, *97*, 206806.

[28] P. Daubinger, J. Kieninger, T. Unmussig, G. A. Urban, *Phys. Chem. Chem. Phys.* **2014**, *16*, 8392.

[29] F. de la Peña, E. Prestat, V. Tonaas Fauske, P. Burdet, T. Furnival, P. Jokubauskas, J. Lähnemann, M. Nord, T. Ostasevicius, K. E. MacArthur, D. N. Johnstone, M. Sarahan, J. Taillon, T. Aarholt, V. Migunov, A. Eljarrat, J. Caron, T. Poon, S. Mazzucco, B. Martineau, S. Somnath, T. Slater, C. Francis, N. Tappy, M. Walls, N. Cautaerts, F. Winkler, G. Donval, v1.6.4 ed., Zenodo, **2021**.

[30] J. D. Hunter, *Comput. Sci. Eng.* **2007**, *9*, 90.

[31] S. Jung, C. C. L. McCrory, I. M. Ferrer, J. C. Peters, T. F. Jaramillo, *J. Mater. Chem. A* **2016**, *4*, 3068.

[32] a) U. Hohenester, A. Trügler, *Comput. Phys. Commun.* **2012**, *183*, 370; b) U. Hohenester, *Comput. Phys. Commun.* **2014**, *185*, 1177; c) J. Waxenegger, A. Trügler, U. Hohenester, *Comput. Phys. Commun.* **2015**, *193*, 138.

[33] a) D. W. Lynch, R. Rosei, J. H. Weaver, *Solid State Commun.* **1971**, *9*, 2195; b) A. Rohatgi, WebPlotDigitizer, Pacifica, CA, USA **2021**; c) J. R. Rumble, *CRC Handb. Chem. phys.*, CRC Press, Boca Raton, FL **2017**.

[34] a) P. B. Johnson, R. W. Christy, *Phys. Rev. B* **1972**, *6*, 4370; b) P. B. Johnson, R. W. Christy, *Phys. Rev. B* **1974**, *9*, 5056.